^{10}B + α reactions at low energies

A. Gula,* R. J. deBoer,† S. Aguilar, J. Arroyo, C. Boomershine, B. Frentz, J. Görres, S. Henderson, R. Kelmar, S. McGuinness, K. V. Manukyan, S. Moylan, D. Robertson, C. Seymour, Shahina, E. Stech, W. Tan, J. Wilkinson, and M. Wiescher
Department of Physics and the Joint Institute for Nuclear Astrophysics, University of Notre Dame, Notre Dame, Indiana 46556, USA

(Received 2 November 2022; accepted 3 February 2023; published 22 February 2023)

Nucleosynthesis in primordial stellar environments may lead to a substantial production of ^{10}B isotopes, which either are converted by the ^{10}B$(p,\alpha)^{7}$Be reaction to ^{7}Be or processed further by ^{10}B$+\alpha$ reactions towards the carbon, nitrogen, and oxygen range. This paper focuses on low energy studies of the ^{10}B$(\alpha,p)^{13}$C and ^{10}B$(\alpha,d)^{12}$C reactions to determine the low energy cross section and the reaction rates in stellar environments using *R*-matrix analysis techniques. The experimental results cover a broad energy range, from 0.21 MeV up to 1.4 MeV in the center of mass frame, extending down to the Gamow energy range. A substantial increase in the reaction rate compared to previous predictions is found, due to the identification of near threshold α-cluster resonance structures.

DOI: 10.1103/PhysRevC.107.025805

I. INTRODUCTION

Carbon enhanced metal poor (CEMP) stars are one of the oldest classes of stellar objects in our universe. The observed abundance distributions of these stars reflect a history of complex nucleosynthesis patterns that are based on reaction sequences fueled by the primordial composition of the first generation of stars [1,2]. The critical step for nucleosynthesis is bridging the mass instability gap at $A = 5$ and $A = 8$, which inhibits the reaction flow towards heavier elements in the big bang nucleosynthesis environment [3,4]. The oldest observed stars indeed indicate a pronounced enhancement in carbon and oxygen abundances, suggesting a considerable mass flow from the primordial hydrogen, deuterium, helium, and lithium abundances towards the carbon, nitrogen, and oxygen (CNO) mass range [5,6].

Based on these observations, it was suggested that the first generation of stars typically had masses of 100s or 1000s of $M_{\odot}$, because higher mass stars would have ended as pair-production supernovae instead of core-collapse supernovae, leaving no massive remnant such as a neutron star or black hole but converting large fractions of the primordial abundances into iron [7,8]. Detailed nucleosynthesis simulations for the H- and He-rich burning layers in primordial stars have been recently performed that will impact the abundance distribution of the ejecta of a presupernova event [9]. The JINA Reaclib database (Cyburt *et al.* [10]) has been used for these simulations, however some of the critical rates of reactions coupling the He-Li abundances to the CNO range were rather outdated and based on insufficient theory or experimental data [11].

Besides the triple-α process, additional reaction links need to be considered [12]. Of particular interest is the reaction path ^{2}H$(\alpha,\gamma)^{6}$Li$(\alpha,\gamma)^{10}$B$(\alpha,d)^{12}$C in these primordial stellar environments. It represents a reaction cycle, since a fraction of the reaction products are being recycled back into the initial deuterium seed material, maintaining a larger deuterium supply than initially anticipated [12]. This reaction chain could run at lower temperatures than the 3α process, unless proton-induced reactions such as ^{6}Li$(p,\alpha)^{3}$He or ^{10}B$(p,\alpha)^{7}$Be divert material back towards lighter masses [13]. For a reliable simulation, the rates of all of the associated reactions need to be well known to determine the strength of the mass flow through this reaction link. The required level of accuracy depends on the level of uncertainty in the observational data and the quality of the model used to predict the impact of the reaction rate. In this case, we strive for an accuracy of $\approx$20% based on the quality of the experimental data and the *R*-matrix analysis. This is expected to improve substantially over previous estimates of the reaction rate by Wagoner [11], which was based on generic assumptions of the associated nature and strength of the nuclear reaction component which at best limits the uncertainty to an order of magnitude range. Not considered earlier in this reaction chain is the strong resonance structures in the cross section, which appear very close to the thresholds of the reaction chain processes [14–17]. Such broad resonances have also been observed in recent studies of the ^{10}B$(\alpha,n)^{13}$N branch as a possible neutron source in primordial stars [18,19]. These strong resonant structures near the threshold are currently believed to represent α-cluster states in the respective compound nuclei ^{6}Li, ^{10}B, and ^{14}N, such as those postulated by Ikeda [20,21]. It has been proposed that such cluster features are a consequence of the collective coupling of shell-model states via the decay channel that leads to the formation of the cluster state [22,23]. An investigation of the impact of these cluster resonances on the reaction chain is necessary to accurately determine the possible primordial

*Present address: ISR-1, ISR Division, Los Alamos National Laboratory, PO Box 1663, Los Alamos, NM 87545, USA.
†rdeboer1@nd.edu

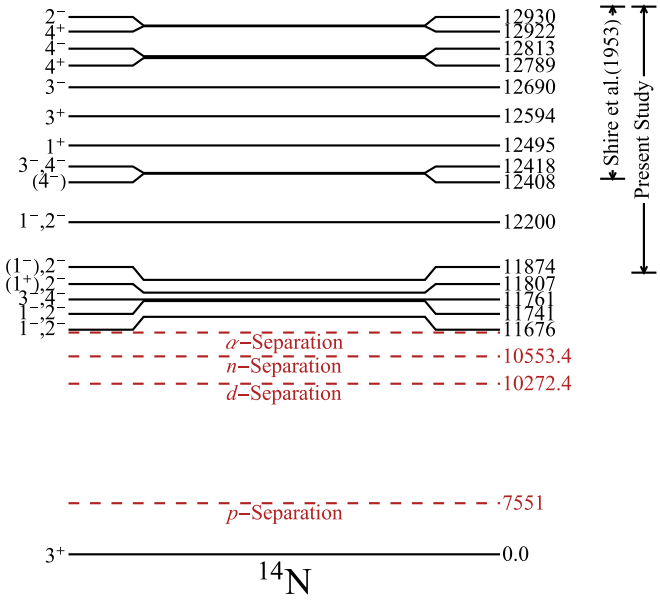

FIG. 1. Level scheme of the ^{14}N compound nucleus as taken from [33]. The α separation ($S_\alpha = 11612$ keV), neutron separation ($S_n = 10553.4$ keV), deuteron separation ($S_d = 10272.4$ keV), and proton separation ($S_p = 7551$ keV) energies are shown in red. The energy range of the previous study is shown alongside the current energy range explored in the present study. Many broad resonance features are present close to the α-separation threshold, which could greatly enhance the low energy cross section and thus the reaction rate.

abundance enrichment of CNO elements in the first and second generations of stars. In this work we will concentrate on the study of α-induced reactions on ^{10}B feeding different isotopes in the CNO range.

The importance of the $^{10}\mathrm{B}(\alpha, d)\,^{12}\mathrm{C}$ reaction is twofold. It produces additional deuterium fuel by reprocessing some of the primordial deuterium abundance through the $^{2}\mathrm{H}(\alpha, \gamma)\,^{6}\mathrm{Li}(\alpha, \gamma)\,^{10}\mathrm{B}(\alpha, d)\,^{12}\mathrm{C}$ reaction chain while producing CNO elements. Limitations on the production of deuterium from this reaction, such as leakage or destruction

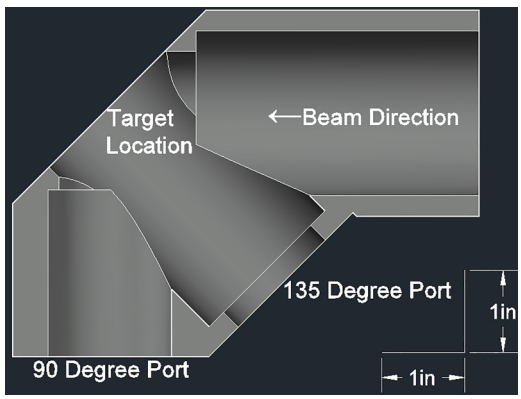

FIG. 2. Cross section of the target chamber. The solid aluminum target chamber has two detector ports located at 90° and 135°. The target is placed at 45° with respect to the beam direction.

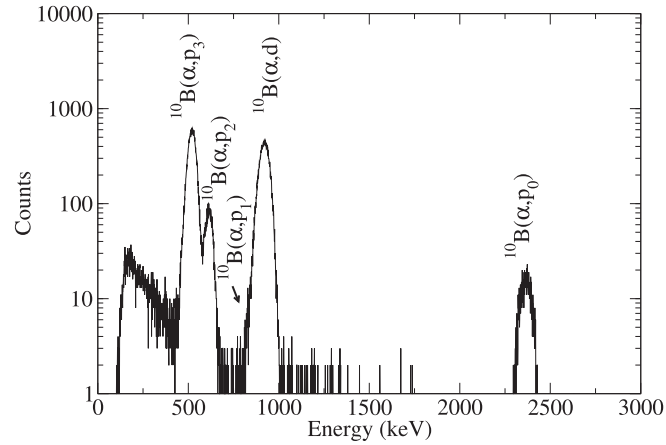

FIG. 3. Sample spectrum for the $\theta_{\mathrm{lab}} = 90°$ SSBD at $E_{\alpha\text{-c.m.}} = 1.2$ MeV. The various peaks correspond to charged particles from the $^{10}\mathrm{B} + \alpha$ reactions. The peaks are more poorly resolved in this detector compared to that at $\theta_{\mathrm{lab}} = 135°$, due to the reaction kinematics. In particular, the peaks corresponding to the $^{10}\mathrm{B}(\alpha, p_1)\,^{13}\mathrm{C}^*$ and $^{10}\mathrm{B}(\alpha, d)\,^{12}\mathrm{C}$ reactions cannot be easily resolved, thus no $^{10}\mathrm{B}(\alpha, d)\,^{12}\mathrm{C}$ yields were acquired from this detector. $^{10}\mathrm{B}(\alpha, p_2/p_3)\,^{13}\mathrm{C}^*$ yields were acquired until they fell below the detector threshold at $E_{\alpha\text{-c.m.}} \approx 640$ keV.

of ^{10}B by proton or neutron induced processes, limit the creation of CNO elements in these early environments. The abundance of ^{10}B seed material in primordial environments is very low and present upper limits for ^{10}B are around 10^{-16} number fraction of metals with respect to hydrogen [24]. This abundance is determined by the feeding of ^{10}B via α capture on ^{6}Li and by depletion via the proton-induced $^{10}\mathrm{B}(p, \alpha)^{7}\mathrm{Be}$ reaction [25]. The latter feeds the material back into the primordial mass range, while the α-particle induced reaction processes, namely, $^{10}\mathrm{B}(\alpha, p)\,^{13}\mathrm{C}$ and $^{10}\mathrm{B}(\alpha, n)\,^{13}\mathrm{N}$ [18,26–28], also provide different links to CNO elements.

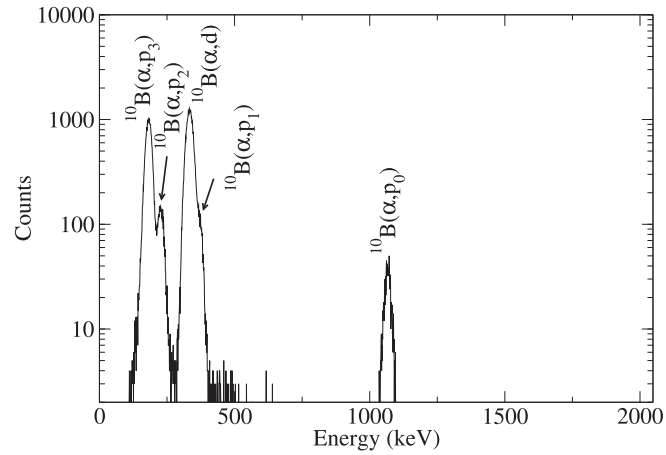

FIG. 4. Sample spectrum from the $\theta_{\mathrm{lab}} = 135°$ SSBD at $E_{\alpha\text{-c.m.}} = 1.2$ MeV. The charged particles from the $^{10}\mathrm{B}(\alpha, d)\,^{12}\mathrm{C}$ and $^{10}\mathrm{B}(\alpha, p_1)\,^{13}\mathrm{C}^*$ reactions are more clearly separable in the this detector than in the $\theta_{\mathrm{lab}} = 90°$ detector. This separation was sufficient for yield separation using a Gaussian fitting algorithm.

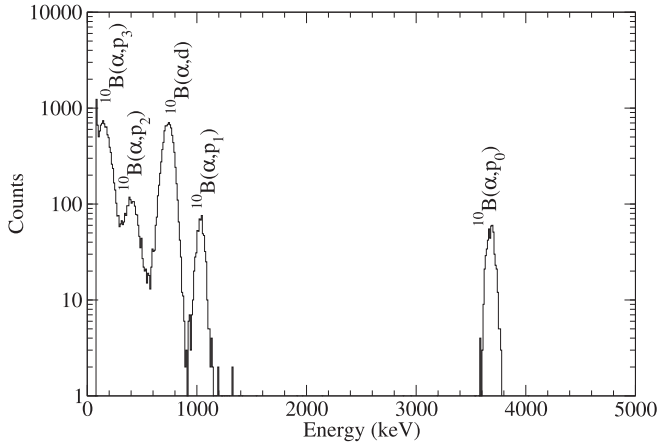

FIG. 5. Sample spectrum from the $\theta_{\text{lab}} = 135^\circ$ SSBD at $E_{\alpha\text{-c.m.}} =$ 1.2 MeV. The charged particles from the $^{10}\text{B}(\alpha, d)\,^{12}\text{C}$ and $^{10}\text{B}(\alpha, p_1)\,^{13}\text{C}^*$ reactions are more clearly separable, as is accrued damage from x rays.

Additionally, the neutron channel provides an early neutron source to fuel a weak *s* process, which could contribute material to "CEMP-s" stars [1,2,19,29–31].

Additionally, uncertainties in the $^{10}\text{B}(\alpha, p)\,^{13}\text{C}$ reaction rate are also critical for modeling the *νp* process [28,32]. It has been demonstrated in Wanajo *et al.* [32] and Zhang *et al.* [28], that errors in the $^{10}\text{B}(\alpha, p)\,^{13}\text{C}$ reaction rate between 1.5–5 GK have a significant impact on the simulated abundances of p nuclei in the $A = 70$–110 mass range (see Fig. 14 in Wanajo *et al.* [32]). While there are several studies that extend into the higher energy ranges (see Zhang *et al.* [28], and references therein), the data at low energies are very limited.

For the above astrophysical environments, the energy range of interest extends from ≈170 keV up to the MeV range. There is only a single previous low-energy study of $^{10}\text{B} + \alpha$ reactions by Shire *et al.* [26], who measured down to a center of mass energy of 0.7 MeV. Though this prior study yielded important structure information, it was energy-resolution limited. Further, the poor presentation of the data and lack of experimental data tables make these measurements of limit use for reanalysis. This is sufficient reason to reinvestigate these reactions by itself, but subsequent indirect measurements published after the work of Shire *et al.* [26] have indicated that there are several other lower energy levels [33], as shown in Fig. 1. These levels could correspond to strong resonances in the $^{10}\text{B} + \alpha$ reactions if they have an α-cluster nature, and would thereby strongly effect the low energy reaction rate over the temperature range of interest.

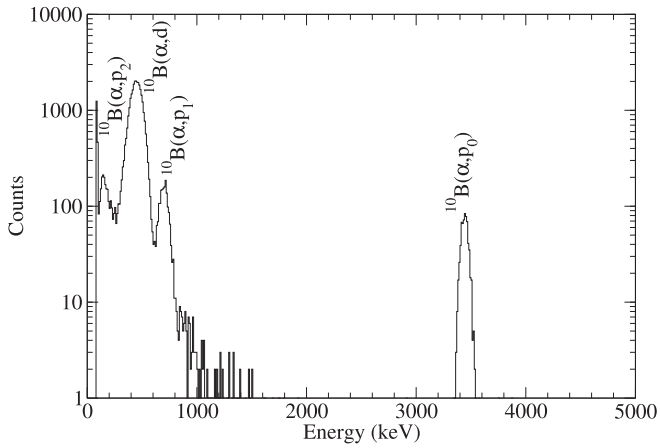

FIG. 6. Sample spectrum of the $\theta_{\text{lab}} = 135^\circ$ SSBD at $E_{\alpha\text{-c.m.}} =$ 0.807 MeV for thick target runs.

TABLE I. Summary of the normalization factors obtained for data from previous works. The paper by Chen *et al.* [44] provided data at only 90°, which required a larger normalization factor, possibly due to angular distribution effects. The rather small normalization factors obtained for the $^{10}\text{B}(\alpha, p\gamma)\,^{13}\text{C}$ data of Liu *et al.* [18] are discussed in the text.

Data set	Ref.	Unc. (%)	Norm.
$^{10}\text{B}(\alpha, n)\,^{13}\text{N}$ @ 0°	Liu *et al.* [18]	12	1
$^{10}\text{B}(\alpha, p_1\gamma)\,^{13}\text{C}$ @ 130°	Liu *et al.* [18]	8	0.54
$^{10}\text{B}(\alpha, p_2\gamma)\,^{13}\text{C}$ @ 130°	Liu *et al.* [18]	8	0.33
$^{10}\text{B}(\alpha, p_3\gamma)\,^{13}\text{C}$ @ 130°	Liu *et al.* [18]	8	0.36
$^{10}\text{B}(\alpha, p_0)\,^{13}\text{C}$ @ 90°	Chen *et al.* [44]	2.6	1.5
$^{10}\text{B}(\alpha, \alpha)\,^{10}\text{B}$ @ 170.5°	McIntyre *et al.* [43]	7	1

α transfer reactions can be used to probe this excitation energy range to search for states with strong α-particle spectroscopic factors, but these measurements are quite limited. In the $^{10}\text{B}(^6\text{Li}, d)^{14}N$ study of Clark and Kemper [34], a clear observation for a state was observed near $E_x = 11.8$ MeV in ^{14}N. As the α-separation energy lies above, but fairly close in energy (≈400 keV) to the deuteron separation energy, $^{12}\text{C} + d$ studies could also be useful in identifying states strongly populated by deuterons. Several $^{12}\text{C}(d, p)\,^{13}\text{C}$ studies [35–37] confirmed the presence of a grouping of resonances that correspond to states in ^{14}N near this $E_x = 11.8$ MeV excitation energy. The combination of these data strongly suggest that there is a state near $E_x = 11.8$ MeV in ^{14}N with a level width (Γ) that is composed of nonzero Γ_α, Γ_d, and Γ_p partial widths.

In this paper we report on a very low energy experimental study of the $^{10}\text{B}(\alpha, p)\,^{13}\text{C}$ and $^{10}\text{B}(\alpha, d)\,^{12}\text{C}$ reactions. The goal of the present study is to search for α-cluster resonances close to the α-particle threshold, improving on the previous measurements of Shire *et al.* [26] and complementing the recent study by Liu *et al.* [18], where the $^{10}\text{B}(\alpha, p\gamma)\,^{13}\text{C}^*$ and $^{10}\text{B}(\alpha, n)\,^{13}\text{N}$ reactions [18] were

TABLE II. AZURE2 experimental effects parameters, which include the number of integration steps per point (Int. Points) and the target density (ρ) (see Refs. [17] and [42]).

Segments	Int. points	ρ (atoms/cm^2)
Thickest targets	50	$3.0(3)\times10^{18}$
Thin targets	20	$8.0(8)\times10^{16}$
Thick targets	20	$6.3(6)\times10^{17}$

TABLE III. Comparison of the widths for the $E_x = 12.69$ and 12.78 MeV states in ^{14}N between the present measurements and those of Shire *et al.* [26] and Liu *et al.* [18]. All widths are given in keV. Note that the level parameters for the $E_x = 12.78$ MeV state were not presented in Liu *et al.* [18] because of significant peak shape distortion from energy loss effects. Uncertainties stem from the statistical and common systematic uncertainty of the experimental data. An additional 5% uncertainty, not included in the values below, is estimated for the simulation of the experimental resolution.

^{14}N* state (MeV)	Study	Γ_α	Γ_n	Γ_{p0}	Γ_{p1}	Γ_{p2}	Γ_{p3}	Γ_d	Γ_{Total} [26]
12.6881	Shire *et al.* [26]	1.7	4.3	0.62	0.17	0.70	5.6	0.93	14(4)
	Present study	2.166(74)	4.50(22)	1.296(44)	0.495(20)	0.553(14)	3.71(14)	2.602(94)	15.32(77)
	Liu *et al.* [18]	5.9	1.9	0.28	0.27	1.9	7.2	0.43	18
12.7844	Shire *et al.* [26]	1.0	0.59	0.18	0.085	0.44	9.6	2.0	14(4)
	Present study	1.764(74)	0.257(21)	0.2138(87)	0.0603(29)	0.0148(28)	6.285(45)	3.037(29)	11.63(58)

investigated. Further, it is important to have data that constrain all of the different exit channels for the ^{10}B $+\alpha$ reactions in order to provide improved constraints for the R-matrix fits, which are used to extrapolate the cross sections to even lower energies.

Section II will describe the experimental setup for the measurements, followed in Secs. III and IV by the analysis of the data and its interpretation in the framework of multichannel R-matrix theory, respectively. Section V describes the calculation of the reaction rates while some conclusions, in terms of the impact on the reaction path in first star environments, will be drawn in Sec. VI.

II. EXPERIMENTAL METHODS

Using the Stable ion Accelerator for Nuclear Astrophysics (Sta. ANA) at the University of Notre Dame, α-particle beams ranging in energy from $E_{\alpha\text{-c.m.}} = 186$ keV–1.43 MeV were produced with intensities ranging from 0.5 to 120 μA on target. Enriched ^{10}B targets with thicknesses, ranging in thickness from ≈4–40 μg/cm^2, were produced by evaporation onto 0.5 mm thick tantalum backings, which also served as a beam stop. To prevent beam-stop failure, this backing was water cooled, which also prevented targets from deteriorating quickly by thermal effects such as the diffusion of target material into the backing. Enrichment in ^{10}B was quoted to be >99.8%, though some contaminant yields from the ^{11}B$(\alpha, p)\,^{14}$C reaction were observed in the region from $E_{\alpha\text{-c.m.}} = 440$–460 keV, owing to the strong, narrow, resonance in that reaction at $E_{\alpha\text{-c.m.}} = 444.4(4)$ keV [38].

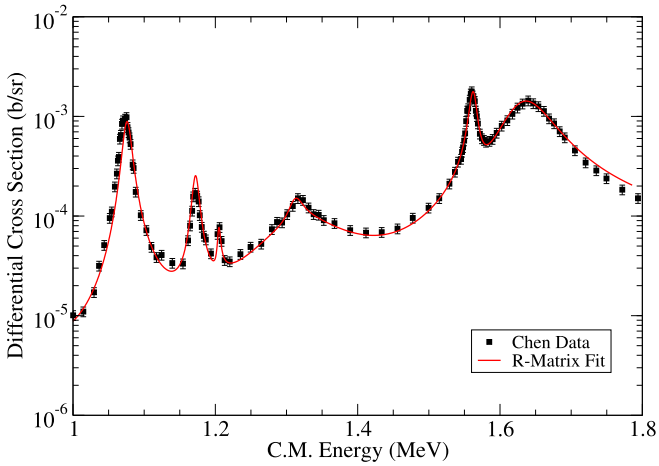

FIG. 7. The R-matrix fit of the ^{10}B$(\alpha, p_0)\,^{13}$C data of Chen *et al.* [44] ($\theta_{\text{lab}} = 90°$). A shift of −7 keV was required to fit this data.

Typically, targets survived between 1–2 C of charge deposition from the helium beam before being gradually degraded by 10–30 %. Once a target had degraded by about 25%, it was replaced with a fresh target of similar thickness. Additionally, before a target was removed or whenever a new target was put in place, a resonance scan was performed. Depending on the thickness of the target, one of the resonances at either $E_{\alpha\text{-c.m.}} = 0.807$, 1.08, or 1.2 MeV, in the ^{10}B(α, d) reaction, were chosen for normalization. The resonance scans provided a target thickness or a normalization from one target to another, allowing for consistency across a wide range of energies and target thicknesses.

The target chamber was machined out of a solid block of aluminum with view ports for two silicon surface barrier detectors (SSBD) located at 90° and 135°. See Fig. 2 for a technical drawing of the target chamber. The target material was mounted on a brass target holder with a steel circular bracing. This target holder was oriented with the water cooling lines leaving transverse to the surface of the chamber. The holder was mounted on the front 45° angled face of the target chamber. Background measurements of this chamber, before and after the experiment, indicated no presence of α-emitting radioactive nuclei above natural background.

Charged particles from the ^{10}B$(\alpha, p_0)\,^{13}$C, ^{10}B$(\alpha, p_1)\,^{13}$C*, and ^{10}B$(\alpha, d)\,^{12}$C reactions were detected using two 100 mm^2 silicon surface barrier detectors (SSBDs), Mode No.1 Bu-013-100-100 [39], placed 6.2 cm from the target at 90° and 135°. Typical intrinsic detection resolution for the protons was better than 20 keV. A removable collimator was placed before each SSBD to reduce the detection rates at high energies. A 1 mm thick aluminum collimator with a 1 cm wide circular aperture was used. One or more ≈7 μm thick aluminum degrader foils were placed in front of the detectors to block the backscattered α-beam particles. Varying numbers of these foils were employed throughout the experimental energy range in order to optimize resolution for maximal particle peak separation. The detection resolution was dominated by the effects of the aluminium foil, which varied substantially

TABLE IV. *R*-matrix particle pair parameters.

Light particle	Heavy particle	Excitation energy (MeV)	Separation energy (MeV)	Channel radius (fm)
α	^{10}B	0	11.6122	5
n	^{13}N	0	10.5534	5
p	^{13}C	0	7.551	5
p	^{13}C	3.08944	7.551	5
p	^{13}C	3.68451	7.551	5
p	^{13}C	3.85381	7.551	5
^{2}H	^{12}C	0	10.2723	5

with outgoing particle energy, but was typically a few tens of keV.

For thin targets (4–12 μg/cm^3) typically one degrader foil was used in front of the SSBD. Example spectra for the charged particle detectors positioned at $\theta_{\text{lab}} = 90^\circ$ and 135° are shown for $E_{\alpha\text{-c.m.}} = 1.2$ MeV in Figs. 3 and 4, respectively. In these thin target runs, proton yields from the ^{10}B$(\alpha, p_1)\,^{13}$C (p_1) and ^{10}B$(\alpha, d)\,^{12}$C (d) reactions were not acquired due to the nearly complete overlap of their respective charged particle peaks. Because of this, additional degrader foils were necessary in order to separate these peaks.

For thick targets (40 μg/cm^3) two degrader foils were used. Example spectra showing separated p_1 and d channels are presented in Figs. 5 and 6, corresponding to the $E_{\alpha\text{-c.m.}} = 1.2$ MeV and $E_{\alpha\text{-c.m.}} = 0.807$ MeV resonances, respectively. In these runs with two degrader foils, the p_1 and d channels are clearly separable, allowing for experimental yields to be acquired. Some x-ray damage to the SSBD is apparent at lower energies resulting from the prior experiments with the thin targets.

III. DATA ANALYSIS

Raw yields for the ^{10}B$(\alpha, p)\,^{13}$C and ^{10}B$(\alpha, d)\,^{12}$C reactions were determined by integrating the regions of interest surrounding the peak and subtracting a time-weighted cosmic ray and detector noise background in the region of interest. In order to acquire the yield for each channel at low energy, centroids and peak widths were acquired for all energies where they were available. Using this information, a trend of the energy for each particle could be determined, even when statistics were low. Whenever two particle channel peaks' left-right bounds came within ten channels, a Gaussian fit was applied to each with an exponential detector background as described below.

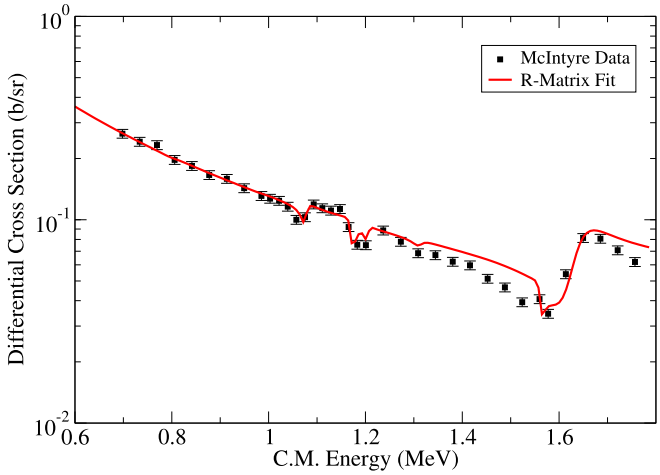

FIG. 8. The *R*-matrix fit to the ^{10}B$(\alpha, \alpha)\,^{10}$B data of McIntyre *et al.* [43] ($\theta_{\text{lab}} = 170.5^\circ$). No adjustments were required for this data.

During the thick target experiments, background measurements were made both before the start of the experiment and after the conclusion. Both background runs were 2.5 d long and showed very little variation in the background rates. This indicated that no significant radioactive contamination was produced in the target chamber nor on the detector surface. This also indicated that no appreciable damage to the detectors was sustained throughout the experiment.

Additionally, the background runs showed that there were very few counts in the region of interest corresponding to the ^{10}B$(\alpha, p_0)\,^{13}$C reaction ($Q = 4.06$ MeV). However, this was not the case very near the threshold of the detector, where the other particle peaks from both the ^{10}B$(\alpha, p_1/p_2/p_3)\,^{13}$C* and ^{10}B$(\alpha, d)\,^{12}$C reactions occurred. A background count rate of ≈400 cts/day was recorded in this region, which had a shape that was well described by a exponential function that decreased at increasing detection energies. This background rate caused particular difficulty in extracting yields for these reactions at very low bombarding energies.

Despite these complications, yields for the ^{10}B$(\alpha, d)\,^{12}$C reaction were obtained down to $E_{\alpha\text{-c.m.}} = 260$ keV. Additional measurements were made down to $E_{\alpha\text{-c.m.}} = 186$ keV, but accurate yields for this reaction could not be determined due to the high uncertainties resulting from large numbers of background events. Upper limits for these runs can be found in Ref. [17].

Using the Monte Carlo N-particle (MCNP) code [40], a geometry of the target chamber with the SSBD was created. The efficiency for each SSBD was determined for protons and

TABLE V. Spin-parity (J^π) assignment differences.

E_x (MeV)	$J^\pi_{\text{Lit.}}$	Ref.	Reaction	J^π_{Current}
11.807	$2^-, (1^+)$	[35,36]	^{12}C(d, p) & ^{12}C(d, d)	3^+
12.922	4^+	[26]	^{10}B(α, x)	2^-
13.255	2^-	[46]	^{10}B$(\alpha, p/n)$	3^+

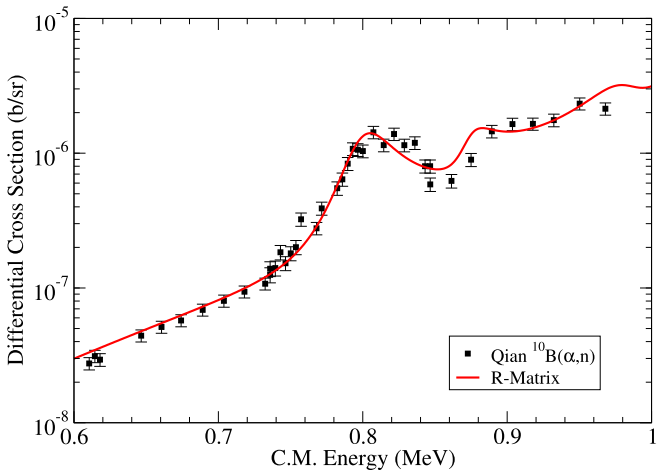

FIG. 9. The *R*-matrix fit to the $^{10}\mathrm{B}(\alpha, n)\,^{13}\mathrm{N}$ data of Liu *et al.* [18] ($\theta_{\mathrm{lab}} = 0^{\circ}$). No adjustments were required for this data.

deuterons. Each simulation was run for 10^8 particles to obtain negligible uncertainty from the statistics of the simulation. Variances on the measured geometries were simulated and a maximum uncertainty of 1.7% in the efficiency was observed. The overall uncertainty in the cross sections also includes that of charge collection (3%) and target thickness (10%), giving a total systematic uncertainty of 11% for the present measurements.

For α-beam energies between $E_{\alpha\text{-c.m.}}$=0.93 and 1.36 MeV, in the laboratory frame, thin targets ($n \approx 8\times10^{16}$ atoms/cm^2) were utilized, as several strong, narrow, resonances were observed in this region. In particular, the 1.2 MeV resonance ($E_x = 12.81$), with $\Gamma \approx 4$ keV, was of interest due to the high degree of uncertainty in its width [26]. In the $E_\alpha =$ 1.2–1.36 MeV energy region, several resonances were expected to be present, corresponding to several levels in the ^{14}N compound nucleus reported in this region [33]. However, only two broad states were located, one at $E_x = 12.924$ MeV and another at $E_x = 12.926$ MeV, corresponding to $E_{\alpha\text{-c.m.}} = 1.312$ and 1.314 MeV, respectively. The significantly broader of these two states, located at $E_x = 12.926$ MeV, was the dominant resonance at $E_\alpha = 1.839$ MeV seen in the $^{10}\mathrm{B}(\alpha, p_1/p_2)\,^{13}\mathrm{C}^*$ reactions. Whereas the level located at $E_x = 12.924$ MeV was found to have considerable strength in the $^{10}\mathrm{B}(\alpha, p_0/p_3)\,^{13}\mathrm{C}^*$ and $^{10}\mathrm{B}(\alpha, d)\,^{12}\mathrm{C}$ reactions at $E_{\alpha\text{-c.m.}} = 1.312$ MeV. Though, the broad underlying resonance corresponding to $E_{\alpha\text{-c.m.}} = 1.314$ MeV also contributed some strength in the $^{10}\mathrm{B}(\alpha, p_0/p_3)\,^{13}\mathrm{C}^*$ and $^{10}\mathrm{B}(\alpha, d)\,^{12}\mathrm{C}$ reactions. A clear distinction in the widths of these resonances can be seen in the *R*-matrix fits presented later in Sec. IV in the $^{10}\mathrm{B}(\alpha, p_2)\,^{13}\mathrm{C}^*$ and $^{10}\mathrm{B}(\alpha, p_3)\,^{13}\mathrm{C}^*$ data.

The excitation function for the $^{10}\mathrm{B}(\alpha, p_3)\,^{13}\mathrm{C}^*$ reaction showed some evidence for a broad underlying state that provides an increase to the yield in between $E_{\alpha\text{-c.m.}} = 0.93$ and 1.36 MeV. This broad structure appears to peak somewhere near $E_{\alpha\text{-c.m.}} = 1.18$ MeV, corresponding to $E_x = 12.78$ MeV in the compound nucleus. This feature is further discussed in Sec. IV.

Below $E_{\alpha\text{-c.m.}} = 0.8$ MeV, all states have been reported to have a width of $\Gamma > 40$ keV [33]. Targets with thicknesses varying between $n \approx 6\times10^{17}$ and $n \approx 3\times10^{18}$ atoms/cm^2 were used to scan this energy range between $E_{\alpha\text{-c.m.}} =$ 0.64 and 1.0 MeV, these thicknesses correspond to energy losses of $\Delta E =$ 20–100 keV at $E_{\alpha\text{-c.m.}} = 0.714$ MeV. The known levels in the region, located at $E_x = 12.40$, 12.42, and 12.489 MeV, have total widths larger than the beam energy loss through these thick targets. Detailed energy scans in this region revealed that only the $E_x = 12.42$ and 12.489 MeV levels contributed resonances at $E_{\alpha\text{-c.m.}} = 800.8$ and 873.7 keV to the charged particle cross sections.

The thickest targets, $n \approx 3\times10^{18}$ atoms/cm^2, corresponding to an energy loss of $\Delta E \approx 100$ keV, were used to scan the entire region of interest: $E_{\alpha\text{-c.m.}} = 0.21$–1.42 MeV. These thick target measurements consisted of high statistics runs measured every ≈3.5 keV throughout the $E_{\alpha\text{-c.m.}} = 0.786$–1.42 MeV energy region. The thickness of these targets allowed for the measurement of the high energy tail from a near-threshold resonance at very low energies observed in the $^{10}\mathrm{B}(\alpha, p_0)\,^{13}\mathrm{C}$ and $^{10}\mathrm{B}(\alpha, d)\,^{12}\mathrm{C}$ reactions. The corresponding level lies below $E_x = 11.85$ MeV in the ^{14}N compound system. It appears likely that this resonance contribution corresponds to the $E_x = 11.807$ MeV state in ^{14}N observed in $^{12}\mathrm{C}+d$ and $^{10}\mathrm{B}(^6\mathrm{Li}, d)\,^{14}\mathrm{N}$ reaction studies [33–36].

IV. *R*-MATRIX ANALYSIS

Using the *R*-matrix data analysis framework, AZURE2 [41,42], fits were performed for the $^{10}\mathrm{B}+\alpha$ reactions reported here. In addition to the data acquired in this study, the $^{10}\mathrm{B}(\alpha, n)\,^{13}\mathrm{N}$ and $^{10}\mathrm{B}(\alpha, p\gamma)\,^{13}\mathrm{C}$ data of Liu *et al.* [18] were included as well as the $^{10}\mathrm{B}(\alpha, \alpha)\,^{10}\mathrm{B}$ elastic scattering data of McIntyre *et al.* [43] and $^{10}\mathrm{B}(\alpha, p)\,^{13}\mathrm{C}$ data of Chen *et al.* [44]. With these data sets, a significantly more comprehensive *R*-matrix analysis of the ^{14}N compound system near the α-particle separation energy was achieved, providing experimental constraint over all open exit channels. The fit included 15 levels and the full set of six open particle channels ($^{10}\mathrm{B}+\alpha$, $^{12}\mathrm{C}+d$, $^{13}\mathrm{C}+p_{1,2,3}$, and $^{13}\mathrm{N}+n$). Numerical issues can be encountered for calculations where a level's total width is small, less than order eV, but this was not the case for any of the levels in the present calculation. A summary of the different normalization factors for each data set are given in Table I. Due to the relatively thick targets used for some portions of the experimental measurements (see Sec. III), energy loss and averaging effects were included using the AZURE2 code's experimental convolution routines as summarized in Table II. The alternative Brune parametrization is used [45] to obtain the observable level energies and partial widths. A comparison with the previous results from Shire *et al.* [26] are given in Table III. Finally, the full list of level parameters from the *R*-matrix fit are given in Table IV of the Appendix.

Through the simultaneous fit performed for all of the α-induced reactions on ^{10}B, an improved analysis of the *R*-matrix level parameters of this energy region was achieved. This represents a substantial improvement over the Breit-Wigner analysis of Shire *et al.* [26] and the *R*-matrix analysis

TABLE VI. Compound nucleus excited state energy comparison. Excitation and laboratory energies are given in MeV.

E_{x} -NNDC [33]	E_{x}-Shire [26]	E_{x}-Liu [18]	E_{x}-Current	E_{α}-NNDC [33]	E_{α}-Shire [26]	E_{α}-Liu [18]	E_{α}-Current
12.418(3)	12.419(7)	12.421(1)	12.413(1)	1.128(4)	1.13(1)	1.132(2)	1.1209(20)
12.495(9)	12.498(7)	12.498(1)	12.489(1)	1.236(13)	1.24(1)	1.240(2)	1.2273(20)
12.594(3)	12.605(7)	12.600(1)	12.596(1)	1.374(4)	1.39(1)	1.383(2)	1.3771(20)
12.690(5)	12.691(7)	12.689(1)	12.688(1)	1.509(7)	1.51(1)	1.507(2)	1.5058(20)
12.789(5)	12.784(7)	12.789(5)	12.785(1)	1.647(7)	1.64(1)	1.647(7)	1.6416(20)
12.813(4)	12.812(7)	12.813(4)	12.817(1)	1.681(6)	1.68(1)	1.681(6)	1.6864(20)
12.922(5)	12.920(7)	12.922(5)	12.925(1)	1.833(7)	1.83(1)	1.833(7)	1.8376(20)

of Liu *et al.* [18], where fewer channels over a narrower energy range were considered due to the lack of experimental data. The fit to the ^{10}B(α, d) ^{12}C data, two separate angles for the ^{10}B(α, p_0) ^{13}C data, and the ^{10}B(α, p_1) ^{13}C data are shown in Figs. 13–16. The data were acquired with the thick targets ($n \approx 3\times10^{18}$) described in Sec. II and use the experimental effect parameters given in the first row of Table II. In the region between $E_{\alpha\text{-c.m.}} = 0.786$–$1.42$ MeV, energy steps of <3.5 keV were taken in order to accurately constrain the high energy region of these cross sections. The S factors for the ^{10}B(α, d) ^{12}C and ^{10}B(α, p_0) ^{13}C reactions are presented in Figs. 19 and 20, respectively, and clearly indicate a strong enhancement at low energies.

The ^{10}B(α, p_2) ^{13}C and ^{10}B(α, p_3) ^{13}C reactions are shown in Figs. 17 and 18. These data were acquired with a combination of targets, depending on the yield requirements at a given energy. The targets used were the thin and thick targets ($\approx8\times10^{16}$ and $\approx6.3\times10^{17}$) described in the experimental effect calculation shown in the last two rows of Table II.

Comparing the present work to that performed recently by Liu *et al.* [18], it appears that the p_3 widths present in Table V of that work are larger than those found here (see Tables VII and VIII). This difference is likely the result of the limited data available at that time for the deuteron channel as well as a possible issue with the absolute normalization of the data. The lack of constraint for all channels could allowed for multiple solutions in the R-matrix fit, demonstrated by the very similar fits shown in Fig. 10 in Liu *et al.* [18] compared to those of this work. Additionally, this can also be seen in the charged particle channels from McIntyre *et al.* [43] and Chen *et al.* [44], which are shown subsequently in Figs. 8 and 7, respectively. These data were also used in the Liu *et al.* [18] study, with very similar fits being acquired here for a larger range of data points. It should also be noted that there is an error in Table V of Liu *et al.* [18] where the p_1 and p_2 widths for the $E_x = 12.4858$ MeV state need to be shifted one column to the right.

The present R-matrix analysis also includes the data from the study by Liu *et al.* [18], first presented in Fig. 9. This data required no normalization or energy shift in order to be fit simultaneously. However, the same was not true for the ^{10}B(α, $p_i\gamma$) ^{13}C data. Though a similar quality fit was obtained here for these data, large normalization factors were required. It was found that normalizations of the ^{10}B(α, p_i) data were 0.54, 0.33, and 0.36, respectively, for p_1, p_2, and p_3 reactions. The reason for this normalization discrepancy is presently unknown, but could be an indication of incorrect spin assignments for some of the levels in the R-matrix fit or could be from an error or poor approximation in the conversion of the secondary γ-ray production cross sections to reaction cross sections in Liu *et al.* [18]. The fits for these data between $E_{\alpha\text{-c.m.}} = 0.6$ and 1 MeV are shown in Figs. 10–12.

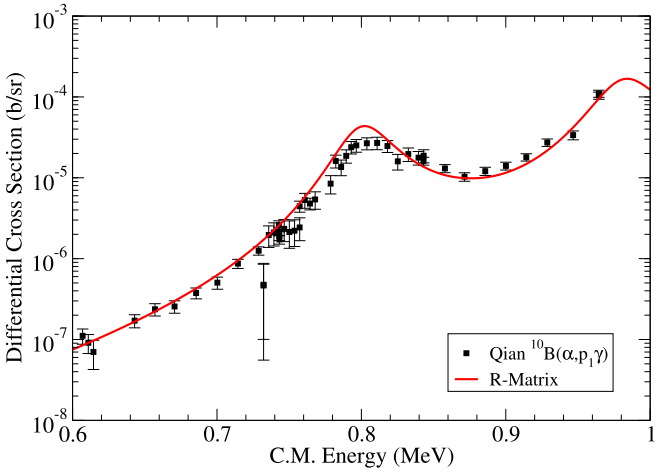

FIG. 10. The R-matrix fit to the ^{10}B(α, p$_1\gamma$) ^{13}C data of Liu *et al.* [18] ($\theta_\gamma = 130°$). A normalization of 0.54 was required to fit this data.

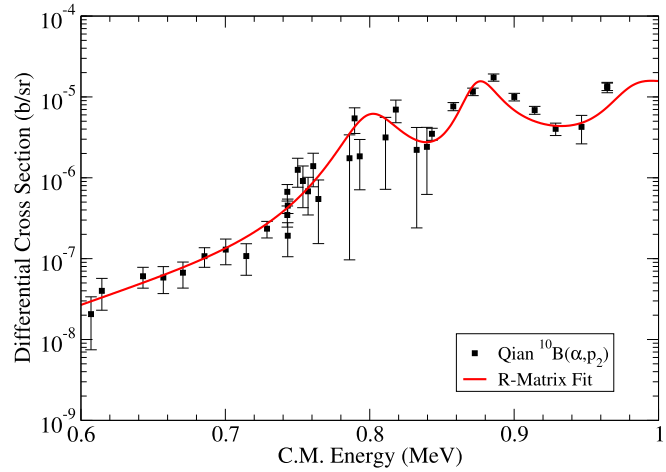

FIG. 11. The R-matrix fit to the ^{10}B(α, p$_2\gamma$) ^{13}C data of Liu *et al.* [18] ($\theta_\gamma = 130°$). A normalization of 0.33 was required to fit this data.

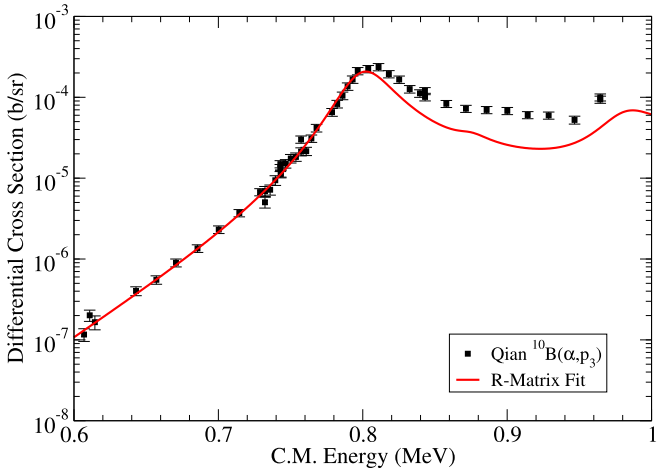

FIG. 12. The *R*-matrix fit to the ^{10}B(α, $p_3\gamma$) ^{13}C data of Liu *et al.* [18] ($\theta_\gamma = 130^\circ$). A normalization of 0.36 was required to fit this data.

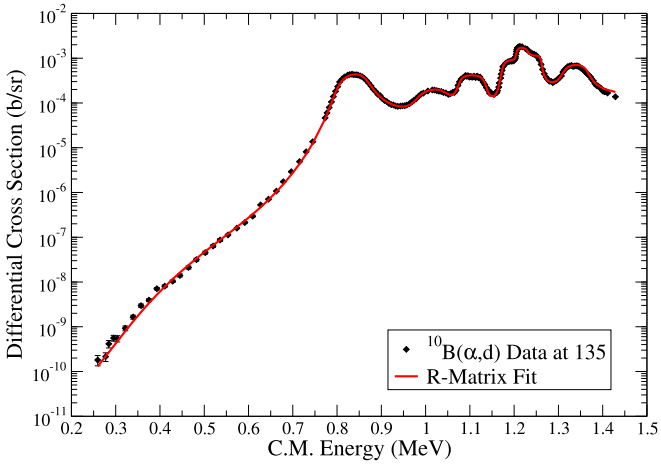

FIG. 13. *R*-matrix fit to the differential data at $\theta_{\rm lab} = 135^\circ$ from the ^{10}B(α, d) ^{12}C reaction between $E_{\alpha-cm} = 0.21$ and 1.42 MeV from the present work.

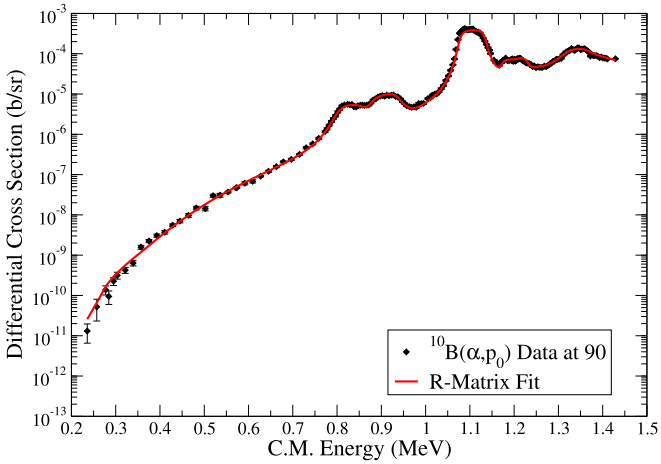

FIG. 14. *R*-matrix fit to the differential data at $\theta_{\rm lab} = 90^\circ$ from the ^{10}B(α, p_0) ^{13}C reaction between $E_{\alpha-cm} = 0.21$ and 1.42 MeV from the present work.

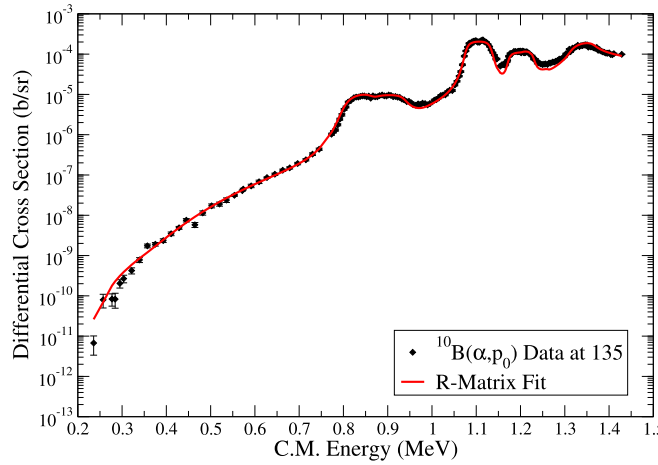

FIG. 15. As Fig. 14, but at $\theta_{\rm lab} = 135^\circ$.

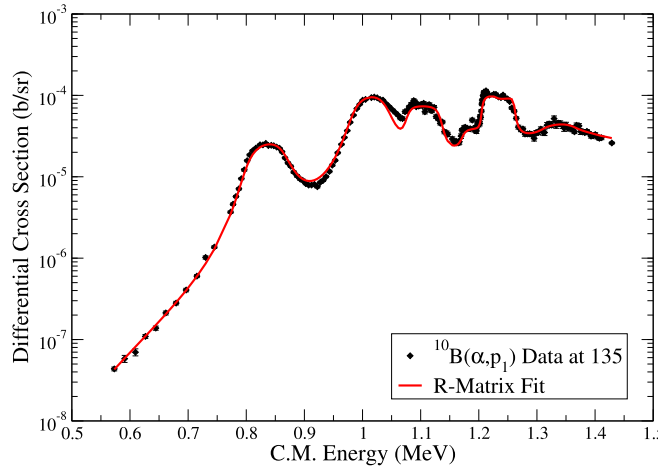

FIG. 16. *R*-matrix fit to the differential data at $\theta_{\rm lab} = 135^\circ$ from the ^{10}B(α, p_1) ^{13}C reaction between $E_{\alpha\text{-c.m.}} = 0.57$ and 1.42 MeV from the present work.

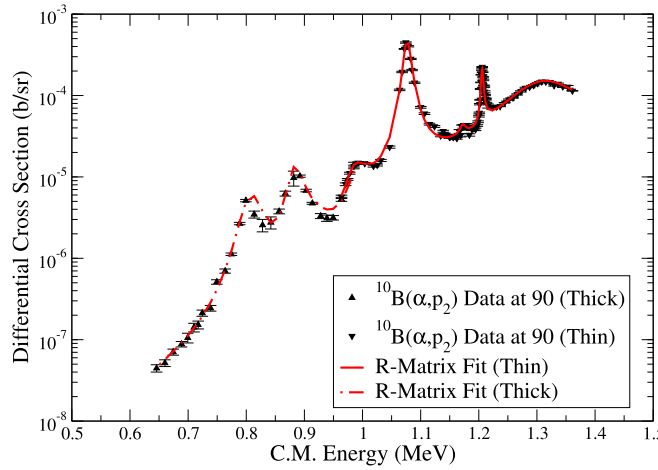

FIG. 17. *R*-matrix fit to the differential data at $\theta_{\rm lab} = 90^\circ$ from the ^{10}B(α, p_2) ^{13}C reaction between $E_{\alpha\text{-c.m.}} = 0.64$ and 1.42 MeV.

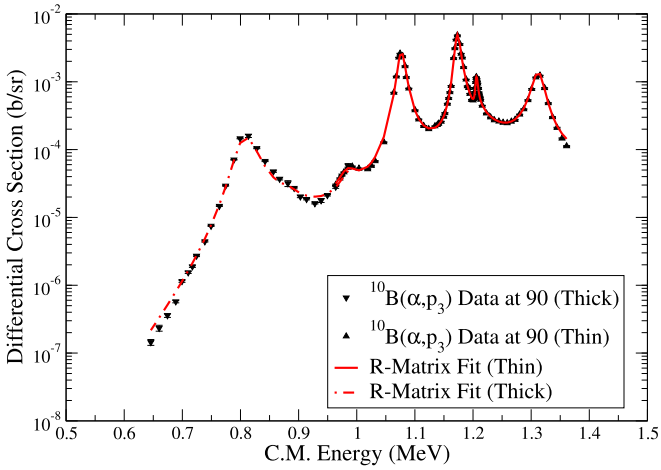

FIG. 18. As Fig. 17, but for the ^{10}B(α, p_3) ^{13}C reaction.

In the work performed by Shire *et al.* [26], it was stated that the resonance widths were determined primarily from the observed widths of the resonances after being corrected by the center-of-mass factor and target thickness corrections. A comparison of the resonance widths derived by Shire *et al.* [26] and obtained in the present *R*-matrix fit is given in the last column of Table III. Differences between the present work and that of Shire *et al.* [26] are attributed to the poorer resolution of that work.

Beyond the errors discovered in the Γ_{p3} and Γ_d widths, additional differences are seen among the other ^{10}B(α, x) reactions. There are several widths that differ by nearly a factor of two. However, this level of discrepancy is still with in the large uncertainty estimated by Shire *et al.* [26].

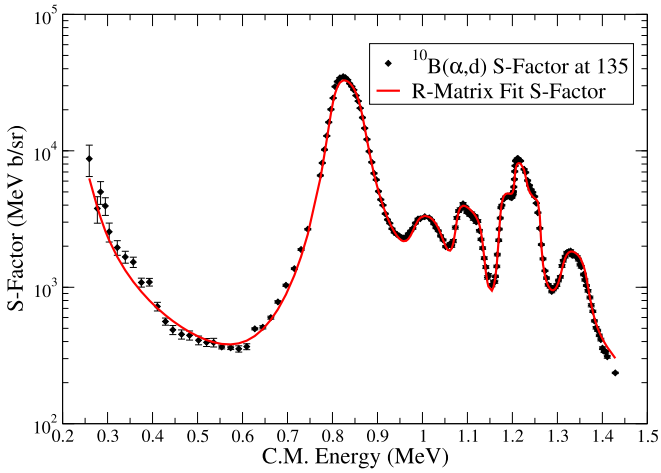

FIG. 19. Differential S factor of the ^{10}B(α, d) ^{12}C reaction between $E_{\alpha\text{-c.m.}} = 0.21$ and 1.42 MeV. Because the present measurement was able to reach very low energies, the existence of a near threshold resonance(s) was discovered. This strong enhancement of the S factor at low energies increases the reaction rate significantly and allows for more deuterium nuclei to be regenerated in low metallicity stars.

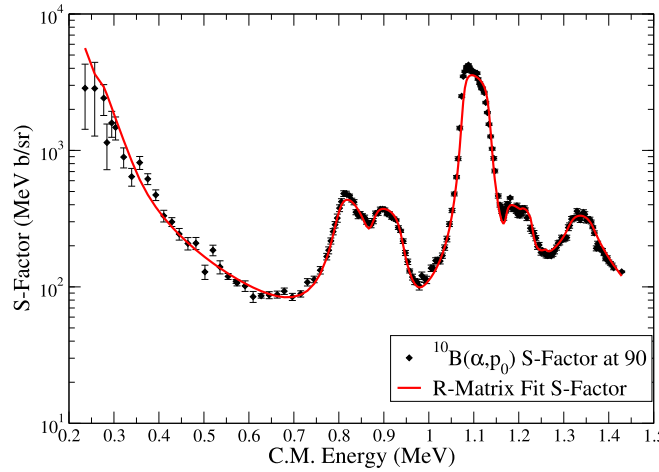

FIG. 20. Differential S factor of the ^{10}B(α, p_0) ^{13}C reaction at $\theta_{\text{lab}} = 90^\circ$ between $E_{\alpha\text{-c.m.}} = 0.21$ and 1.42 MeV. Similar to the ^{10}B(α, d) ^{12}C reaction, strong enhancement at low energies is observed. This enhancement may lead to significant impacts on the nucleosynthesis of heavier nuclei, as demonstrated recently by [28] and [32].

Small energy differences in the excited states are observed in the present study when compared to the evaluated data for ^{14}N [33]. The energy of the resonances observed in the previous measurements of Shire *et al.* [26] and Liu *et al.* [18] are compared to the present study and the current ENSDF literature [33] as shown in Table VI. The previously reported spins and parities of these states were found to be in good agreement with the *R*-matrix fit, with the key exceptions of those at $E_x = 11.807$, 12.922, and 13.255 MeV. These discrepancies are discussed below and are summarized in Table V.

Most of the resonance energies presented in Table VI are consistent with those of Shire *et al.* [26], Liu *et al.* [18], and the compilation [33] within their quoted uncertainties, however the $E_x = 12.413(1)$ MeV state is an exception. As previously mentioned, this state corresponds to a very strong and broad resonance, where accurate determinations of the centroid are obfuscated by nearby resonances and the interference patterns throughout the spectrum. Specifically, the $E_x = 12.489(1)$ MeV resonance observed in the present study has appreciable strength in several charged particle channels reflected in an interference pattern between these two broad resonances. These factors could help explain the ≈5 keV deviation from previous works, where Breit-Wigner analyses did not include energy shifts due to interferences.

The $E_x = 11.807$ MeV state [33] is assumed to be responsible for the near-threshold S-factor enhancement observed in the present data. As shown in Table V, the tentative J^π assignment of 2^-, (1^+) is from (d, p) and (d, d) on ^{12}C [35,36]. However the *R*-matrix fit to the present data favors a spin assignment of 3^+ due to the observed angular dependence in the p_0 channel. This could indicate that a different level is also present near this energy. However, the literature indicates that none of the currently known levels in this region ($E_x < 12$ MeV) have such a J^π assignment [33]. This energy region

(11.2 MeV $< E_x <$ 12.2 MeV) has a particularly complicated resonance structure, see, for example, Fig. 4 of Kashy *et al.* [36], Fig. 3 of Kashy *et al.* [47], and Fig. 6 of Tryti *et al.* [35]. The disagreements in spin-parity assignments in this excitation energy region could be caused by complicated interference patterns of unaccounted for resonances.

As shown in Table V, the $E_x < 12.922$ MeV state has a spin and parity assignment of $J^\pi = 4^+$ from angular distribution measurements by Shire *et al.* [26], though the data are not shown there. However, in the current *R*-matrix fit, a better fit across all channels is found with an assignment of $J^\pi = 2^-$. This discrepancy may also be due to the presence of interference patterns between this resonance and several other broad resonances, such as those corresponding to the ^{14}N levels at $E_x \approx 13.25$, 12.93, and 12.78 MeV.

The final state that appears to be in disagreement with spin-parities found in literature is that at $E_x = 13.255$ MeV with $J^\pi = 2^-$ [15]. However, it appears that the fit to the $^{10}\mathrm{B}(\alpha,\alpha)\,^{10}\mathrm{B}$ scattering data of McIntyre *et al.* [43] is better fit with a $J^\pi = 3^+$ spin and parity assignment. This spin assignment is in accord with that provided in [48]. However, two broad resonances are reported in this region in the literature, one at $E_x = 13.192$ MeV and another at $E_x = 13.243$ MeV with spin assignments of $J^\pi = 3^+$ and $J^\pi = 2^-$, respectively. These spin assignments appear to come from the scattering study of [48] and a later one by [46], respectively. However, in [46], the $E_x \approx 13.25$ MeV state was given a range of (2^+, 2^-, 3^+) but strongly suggested 2^- due to parity considerations. It could be the case that one or both of these states are assigned an incorrect J^π, especially since Wilson [46] considered these resonances together in their analysis of parity considerations. They may have been misled by surrounding resonant contributions, or it could also be the case that the energy for one or both of these levels is incorrect.

V. REACTION RATES

Reaction rates for the α-induced charged-particle reactions were calculated by numerical integration of the *R*-matrix cross sections using AZURE2. The calculations were limited to the temperature range $T = 0.01$–2 GK. Higher temperatures, 2–10 GK, were excluded since significant contributions from higher energy resonances are present that are not considered in the analysis of this work. AZURE2 calculates the reaction rate by adaptive step size integration of the integral [42]

$$N_A\langle\sigma v\rangle = \left(\frac{8}{\pi\mu}\right)^{1/2}\frac{N_A}{(k_\mathrm{B}T)^{3/2}}\int_0^\infty \sigma(E)Ee^{-E/k_BT}dE, \quad (1)$$

where N_A is Avogadro's number, k_B is the Boltzmann constant, T is the temperature, and μ is the reduced mass.

No previous experimentally based calculations of the rate of the $^{10}\mathrm{B}(\alpha,d)\,^{12}\mathrm{C}$ reaction exist in the literature, however, phenomenological estimates have been made for the $^{10}\mathrm{B}(\alpha,p)\,^{13}\mathrm{C}$ reaction (Table 9B in [11]), where the basis for this rate relies on a simple barrier penetration model with a constant *S*-factor approximation as described in [49] and [11]. This reaction rate has been adopted in the current JINA Reaclib database [10].

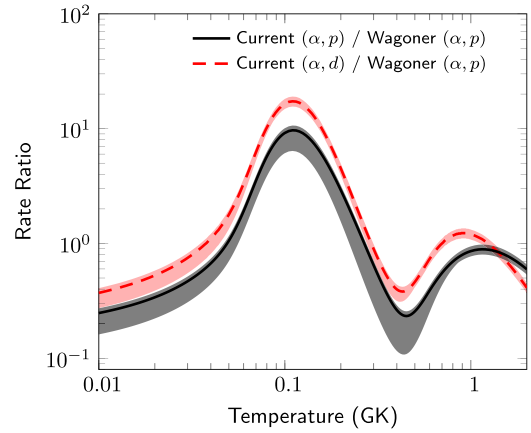

FIG. 21. Rate ratio of the $^{10}\mathrm{B}(\alpha,p)\,^{13}\mathrm{C}$ (red dashed line) and $^{10}\mathrm{B}(\alpha,d)\,^{12}\mathrm{C}$ (black solid line) reactions compared to the $^{10}\mathrm{B}(\alpha,p)\,^{13}\mathrm{C}$ rate found in [11]. The present study finds a large enhancement of the low energy reaction rate, nearing an order of magnitude, in the vicinity of 0.1 GK.

While the rate by [11] assumes a single exit channel and does not take into account any possible resonance contributions, the present rate for the $^{10}\mathrm{B}(\alpha,p)\,^{13}\mathrm{C}$ reaction is based on multiple broad resonances decaying into several exit channels. The rate is the sum of each $^{10}\mathrm{B}(\alpha,p_i)\,^{13}\mathrm{C}$ channel contribution. As expected, large deviations are observed between the two $^{10}\mathrm{B}(\alpha,p)\,^{13}\mathrm{C}$ reaction rates over much of the temperature range. A ratio of the reaction rate calculated in the present study to that presented in [11] is given in Fig. 21.

Figure 21 shows that the $^{10}\mathrm{B}(\alpha,p)\,^{13}\mathrm{C}$ reaction rate found here is enhanced over that of [11] from $T = 0.05$ to 0.25 GK by the presence of the low-energy near-threshold state the $E_x = 11.807$ MeV. This makes the reaction rate at $\approx$0.1 GK nearly an order of magnitude larger than the con-

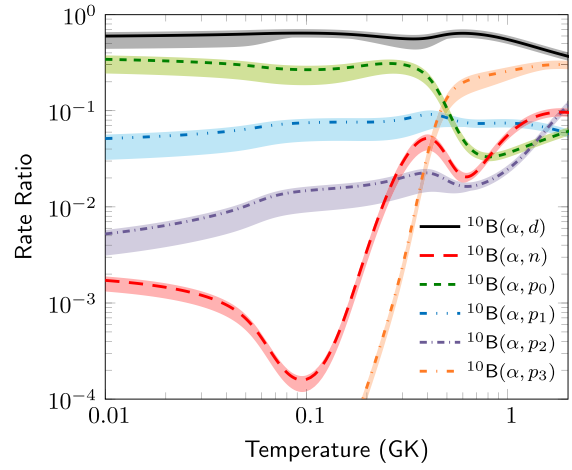

FIG. 22. Branching ratio of the various exit channels of the $^{10}\mathrm{B}+\alpha$ fusion reaction to the total fusion rate as a function of temperature. The present study covers an energy range $E_{\alpha\text{-c.m.}} =$ 0.21–1.42 MeV, which corresponds to stellar temperatures range from 0.01–2 GK.

stant S-factor estimate. This enhancement is also reflected in the ^{10}B$(\alpha, d)\,^{12}$C rate compared to the proton rate from [11].

The strength for each of the exit branches in the ^{10}B $+\alpha$ fusion rate into the different final state configurations is shown in Fig. 22. The ^{10}B$(\alpha, d)\,^{12}$C branch dominates throughout most of the temperature range between 0.01–1 GK, with the ^{10}B$(\alpha, p_0)\,^{13}$C transition playing a more modest role. At higher temperatures, the sum of the proton channels starts to play a more dominant role in feeding the CNO range. The neutron channel plays a negligible role over the entire low temperature range, but at temperatures around 1 GK an appreciable 10% branch is anticipated based on the measurements of [27]. This reaction branch can thus likely be neglected as a potential neutron source in first star burning environments, although it also shows an enhanced S factor at low energies that is not yet well characterized.

The uncertainties in the reaction rates were calculated by taking into account the overall systematic uncertainty of the cross sections measured here (11%) and the uncertainty in the strength of the near threshold state at $E_x = 11.807$ MeV (≈30%, depending on the transition), which dominates the extrapolated cross section. As the level structure below the energy range of the experimental data still remains quite uncertain, additional variation is expected if other levels are found to be present there. Thus, the reaction rate uncertainties are dominated by systematic components, especially below ≈0.4 GK, where the resonances corresponding to the $E_x = 11.807$ MeV dominates the reaction rate for all of the reaction channels. These uncertainties are reflected in Figs. 21 and 22.

VI. CONCLUSION

New measurements for the ^{10}B$(\alpha, d)\,^{12}$C and ^{10}B$(\alpha, p)\,^{13}$C reactions are presented, which include the indication of a very strong near-threshold resonance(s), which may correspond to the similar enhancement observed in the ^{10}B$(\alpha, n)\,^{13}$N study of [18]. Excitation functions for all open charged particle reactions are presented at the lowest energies observed to date, between $E_{\alpha\text{-c.m.}} = 0.21$–$1.42$ MeV or $E_{\alpha\text{-c.m.}} = 0.64$–$1.42$ MeV. Some discrepancies with the prior comprehensive measurements of [26] exist, though they may be explainable given the previous measurement's poorer experimental resolution and the more approximate model used for their cross section fits.

A strong enhancement over the previous estimate by [11] of the ^{10}B$(\alpha, d)\,^{12}$C and ^{10}B$(\alpha, p)\,^{13}$C reaction rates has been observed around $T = 0.1$ GK due to the presence of one or more near-threshold resonances. The energies of these resonances remain unknown, but from the R-matrix fits performed here, and prior literature [34–37], it appears as though these resonances likely corresponds to those reported near $E_x \approx 11.8$ MeV. This suggests that one or more of the states seen in the previous studies of Refs. [34–37] are at play in the ^{10}B $+\alpha$ reactions, all of which could lead to increased CNO element production. The implications due to larger rates for these reactions have been shown to greatly impact primordial stellar burning [13]. Finally, as discussed in [32] and [28], the enhancement of the ^{10}B$(\alpha, p)\,^{13}$C reaction can significantly impact abundances of intermediate mass nuclei ($70 \leqslant A < 110$).

ACKNOWLEDGMENTS

This research utilized resources from the Notre Dame Center for Research Computing and was supported by the National Science Foundation through Grant Nos. PHY-1713857 and PHY-2011890, and the Joint Institute for Nuclear Astrophysics through Grant No. PHY-1430152 (JINA Center for the Evolution of the Elements).

APPENDIX: R-MATRIX LEVEL PARAMETERS

TABLE VII. AZURE2 fit parameters [45] for the ^{10}B $+\alpha$ reaction. Every ℓ (relative orbital angular momentum) and s (channel spin) combination not shown has $\Gamma_x = 0$ and was not included in the fit. Uncertainties stem from the statistical and common systematic uncertainties of the data. An additional 5% uncertainty is recommended for the partial widths from the simulation of the experimental energy resolution. An additional 2 keV uncertainty is common for the energies, corresponding to the uncertainty in the energy calibration of the accelerator. The signs on the partial correspond to the interference sign of the corresponding reduced width amplitude in the R-matrix calculation.

E_x (MeV)	J^π	Channel	ℓ	s	Γ_x (eV)
12.2400[a]	1^-	α	3	3	−0.70(5)
		p_0	0	1	60000(5000)
		p_1	1	0	105000(63000)
		p_3	1	2	15000(3000)
		d	1	1	439000(81000)
12.4858(3)	1^+	α	2	3	25.36(44)
		n	1	1	606(92)
		p_0	1	1	−12740(220)
		p_2	1	1	−9600(180)
		p_3	2	2	4260(430)
12.9300(7)	1^+	α	2	3	−1997(34)
		p_0	1	1	−36660(830)
		p_1	0	1	9000(250)
		p_2	1	1	−72480(780)
		p_3	2	2	9100(3500)
		d	0	1	−13000(650)
13.1787[a]	1^+	α	2	3	5080(500)
		p_0	1	1	−2040(200)
		p_1	0	1	1000(100)
		p_2	1	1	4400(400)
		p_3	2	2	206(20)
11.8740[a]	2^-	α	1	3	$4.61(22)\times10^{-5}$
		p_0	2	1	40000(1500)
		p_2	2	1	400(300)
12.9243(1)	2^-	α	1	3	−1322(52)
		p_0	2	1	−691(29)
		p_1	1	1	14.7(28)
		p_3	1	3	−15890(120)
		d	1	1	−6280(630)

TABLE VII. (*Continued*).

12.7800[a]	2^+	α	2	3	490(20)
		p_1	2	1	−10000(660)
		p_3	0	2	−100000(1400)
12.6881(1)	3^-	α	1	3	2166(74)
		n	2	1	−4500(220)
		p_0	2	1	1296(44)
		p_1	3	0	495(20)
		p_2	2	1	−553(14)
		p_3	1	2	3710(140)
		d	3	1	−2602(94)

[a]Value fixed.

TABLE VIII. *R*-matrix level parameters continued.

E_x (MeV)	J^π	Channel	ℓ	s	Γ_x (eV)
11.8070[a]	3^+	α	0	3	$6.3(6)\times10^{-6}$
		p_0	3	0	8320(200)
		p_1	2	1	−2440(86)
		p_2	1	2	485(20)
		d	2	1	20660(870)
11.9980[a]	3^+	α	0	3	0.00155(15)
		n	3	0	−94000(10000)
12.5953(2)	3^+	α	0	3	−169.7(37)
		n	3	0	−68.8(83)
		p_0	3	0	−152(40)
		p_1	2	1	−22836(220)
		p_2	1	2	−1115(25)
		p_3	0	3	−2860(110)
		d	2	1	−11070(370)
13.2555[a]	3^+	α	0	3	42200(4200)
		n	3	0	274(27)
		p_0	3	0	5350(540)
		p_2	3	1	−29200(3000)
		p_3	2	2	69.4(69)
		d	2	1	6000(420)
12.4129(1)	4^-	α	1	3	289.5(94)
		n	4	0	−15.2(13)
		p_0	4	1	−545(19)
		p_1	3	1	−2003(74)
		p_2	2	2	−363(13)
		p_3	1	3	9130(130)
		d	3	1	26160(150)
12.8173(1)	4^-	α	1	3	577(20)
		p_0	4	1	−27.0(10)
		p_1	3	1	−217.7(80)
		p_2	2	2	−129.6(45)
		p_3	1	3	586.4(88)
		d	3	1	3474(18)
12.7844(1)	4^+	α	2	3	1764(74)
		n	3	1	257(21)
		p_0	3	1	−213.8(87)
		p_1	4	0	60.3(29)
		p_2	3	1	14.8(28)
		p_3	2	2	6285(45)
		d	4	1	−3037(29)

[a]Value fixed.

[1] T. C. Beers and N. Christlieb, Annu. Rev. Astron. Astrophys. **43**, 531 (2005).

[2] S. Bisterzo, C. Travaglio, R. Gallino, M. Wiescher, and F. Käppeler, Astrophys. J. **787**, 10 (2014).

[3] C. Pitrou, A. Coc, J.-P. Uzan, and E. Vangioni, Phys. Rep. **754**, 1 (2018).

[4] R. H. Cyburt, B. D. Fields, K. A. Olive, and T.-H. Yeh, Rev. Mod. Phys. **88**, 015004 (2016).

[5] S. C. Keller, M. S. Bessell, A. Frebel, A. R. Casey, M. Asplund, H. R. Jacobson, K. Lind, J. E. Norris, D. Yong, A. Heger, Z. Magic, G. S. D. Costa, B. P. Schmidt, and P. Tisserand, Nature (London) **506**, 463 (2014).

[6] M. S. Bessell, R. Collet, S. C. Keller, A. Frebel, A. Heger, A. R. Casey, T. Masseron, M. Asplund, H. R. Jacobson, K. Lind, A. F. Marino, J. E. Norris, D. Yong, G. D. Costa, C. Chan, Z. Magic, B. Schmidt, and P. Tisserand, Astrophys. J. Lett. **806**, L16 (2015).

[7] A. Heger and S. E. Woosley, Astrophys. J. **724**, 341 (2010).

[8] S. Hirano, T. Hosokawa, N. Yoshida, H. Umeda, K. Omukai, G. Chiaki, and H. W. Yorke, Astrophys. J. **781**, 60 (2014).

[9] O. Clarkson and F. Herwig, Mon. Not. R. Astron. Soc. **500**, 2685 (2020).

[10] R. H. Cyburt, A. M. Amthor, R. Ferguson, Z. Meisel, K. Smith, S. Warren, A. Heger, R. D. Hoffman, T. Rauscher, A. Sakharuk, H. Schatz, F. K. Thielemann, and M. Wiescher, Astrophys. J. Suppl. Ser. **189**, 240 (2010).

[11] R. V. Wagoner, Astrophys. J. Suppl. Ser. **18**, 247 (1969).

[12] M. Wiescher, J. Görres, S. Graff, L. Buchmann, and F. K. Thielemann, Astrophys. J. **343**, 352 (1989).

[13] M. Wiescher, O. Clarkson, R. J. deBoer, and P. Denisenkov, Eur. Phys. J. A **57**, 24 (2021).

[14] D. Tilley, C. Cheves, J. Godwin, G. Hale, H. Hofmann, J. Kelley, C. Sheu, and H. Weller, Nucl. Phys. A **708**, 3 (2002).

[15] D. Tilley, J. Kelley, J. Godwin, D. Millener, J. Purcell, C. Sheu, and H. Weller, Nucl. Phys. A **745**, 155 (2004).

[16] M. Anders, D. Trezzi, R. Menegazzo, M. Aliotta, A. Bellini, D. Bemmerer, C. Broggini, A. Caciolli, P. Corvisiero, H. Costantini, T. Davinson, Z. Elekes, M. Erhard, A. Formicola, Z. Fülöp, G. Gervino, A. Guglielmetti, C. Gustavino, G. Gyürky, M. Junker, and T. Szücs (LUNA Collaboration), Phys. Rev. Lett. **113**, 042501 (2014).

[17] A. Gula, An Alternative 3α Process: The $^2\mathrm{H}(\alpha,\gamma)^6\mathrm{Li}(\alpha,\gamma)^{10}\mathrm{B}(\alpha,d)^{12}\mathrm{C}$ Reaction in Primordial Stars, Ph.D. thesis, University of Notre Dame, Notre Dame, IN 46556, USA, 2022.

[18] Q. Liu, M. Febbraro, R. J. deBoer, S. Aguilar, A. Boeltzig, Y. Chen, M. Couder, J. Görres, E. Lamere, S. Lyons, K. T. Macon, K. Manukyan, L. Morales, S. Pain, W. A. Peters, C. Seymour, G. Seymour, R. Toomey, B. V. Kolk, J. Weaver *et al.*, Phys. Rev. C **101**, 025808 (2020).
[19] M. Wiescher, R. deBoer, J. Görres, A. Gula, and Q. Liu, Acta Phys. Pol. B **51**, 631 (2020).
[20] K. Ikeda, N. Takigawa, and H. Horiuchi, Prog. Theor. Phys. Suppl. **E68**, 464 (1968).
[21] M. Freer, Rep. Prog. Phys. **70**, 2149 (2007).
[22] J. Okołowicz, W. Nazarewicz, and M. Płoszajczak, Fortschr. Phys. **61**, 66 (2013).
[23] J. Okołowicz, M. Płoszajczak, and W. Nazarewicz, Prog. Theor. Phys. Suppl. **196**, 230 (2012).
[24] F. Iocco, A Search for Population III Stars, Ph.D. thesis, Universita di Napoli "Federico II", 2011.
[25] M. Wiescher, R. J. deBoer, J. Görres, and R. E. Azuma, Phys. Rev. C **95**, 044617 (2017).
[26] E. Shire, J. Wormwald, G. Lindsay-Jones, A. Lunden, and A. Stanley, Philos. Mag. **44**, 1197 (1953).
[27] L. Van Der Zwan and K. Geiger, Nucl. Phys. A **216**, 188 (1973).
[28] L. Y. Zhang, J. J. He, S. Wanajo, D. Dell'Aquila, S. Kubono, and G. Zhao, Astrophys. J. **868**, 24 (2018).
[29] E. M. Burbidge, G. R. Burbidge, W. A. Fowler, and F. Hoyle, Rev. Mod. Phys. **29**, 547 (1957).
[30] J. J. Cowan and W. K. Rose, Astrophys. J. **212**, 149 (1977).
[31] F. Käppeler, R. Gallino, S. Bisterzo, and W. Aoki, Rev. Mod. Phys. **83**, 157 (2011).
[32] S. Wanajo, H.-T. Janka, and S. Kubono, Astrophys. J. **729**, 46 (2011).
[33] F. Ajzenberg-Selove, Nucl. Phys. A **523**, 1 (1991).
[34] M. Clark and K. Kemper, Nucl. Phys. A **425**, 185 (1984).
[35] S. Tryti, T. Holtebekk, and F. Ugletveit, Nucl. Phys. A **251**, 206 (1975).
[36] E. Kashy, R. R. Perry, and J. R. Risser, Phys. Rev. **117**, 1289 (1960).
[37] L. Csedreki, I. Uzonyi, G. Sziki, Z. Szikszai, G. Gyurky, and A. Z. Kiss, Nucl. Instrum. Methods Phys. Res. B **328**, 59 (2014).
[38] T. R. Wang, R. B. Vogelaar, and R. W. Kavanagh, Phys. Rev. C **43**, 883 (1991).
[39] ULTRA and ULTRA AS I-on Implated-Silicon Charge-Particle Detectors.
[40] T. Goorley, M. James, T. Booth, F. Brown, J. Bull, L. J. Cox, J. Durkee, J. Elson, M. Fensin, R. A. Forster, J. Hendricks, H. G. Hughes, R. Johns, B. Kiedrowski, R. Martz, S. Mashnik, G. McKinney, D. Pelowitz, R. Prael, J. Sweezy *et al.*, Nucl. Technol. **180**, 298 (2012).
[41] R. E. Azuma, E. Uberseder, E. C. Simpson, C. R. Brune, H. Costantini, R. J. de Boer, J. Görres, M. Heil, P. J. LeBlanc, C. Ugalde, and M. Wiescher, Phys. Rev. C **81**, 045805 (2010).
[42] E. Uberseder and R. J. deBoer, AZURE2 user manual (2015).
[43] L.C. McIntyre, Jr., J. A. Leavitt, M. D. Ashbaugh, Z. Lin, and J. O. Stoner, Jr., Nucl. Instrum. Methods Phys. Res. B **64**, 457 (1992).
[44] H. Chen, X. Wang, L. Shao, J. Liu, A. Yen, and W. Kan Chu, Nucl. Instrum. Methods Phys. Res. B **211**, 1 (2003).
[45] C. R. Brune, Phys. Rev. C **66**, 044611 (2002).
[46] S. J. Wilson, Phys. Rev. C **11**, 1071 (1975).
[47] E. Kashy, R. R. Perry, R. L. Steele, and J. R. Risser, Phys. Rev. **122**, 884 (1961).
[48] T. Mo and H. R. Weller, Phys. Rev. C **8**, 972 (1973).
[49] R. V. Wagoner, W. A. Fowler, and F. Hoyle, Astrophys. J. **148**, 3 (1967).